DOI: 10.13009/EUCASS2025-243
11TH EUROPEAN CONFERENCE FOR AERONAUTICS AND SPACE SCIENCES (EUCASS)

Performance Assessment of an H_2O_2/H_2 Bipropellant Thruster for Innovative Water-based Space Propulsion

Fabio Faraoni[⋆†], *Alberto Sarritzu*[⋆], *Angelo Pasini*[⋆]
[⋆]*University of Pisa, Department of Civil and Industrial Engineering*
Via Girolamo Caruso 8, 56122, Pisa, Italy
fabio.faraoni@phd.unipi.it · alberto.sarritzu@ing.unipi.it · angelo.pasini@unipi.it
[†]Corresponding author

Abstract

In pursuit of innovative, water-based space propulsion, a 200 N bipropellant thruster based on high-concentration hydrogen peroxide (H_2O_2) and hydrogen (H_2) is under development as part of the European project Green SWaP (Green Solar-to-propellant Water Propulsion). In this work, theoretical rocket performance analysis predicts improvements in specific impulse over hydrazine-based bipropellants and other typical green propellant combinations, as well as improvements in density-specific impulse and lower stoichiometric combustion temperatures compared to conventional water electrolysis propulsion. The potential autoignition between H_2O_2 decomposition products and gaseous H_2 is investigated via 0D kinetics simulations, comparing ignition delays with residence times. Additionally, this work reports the developments of simplified transient models for radiative, heat-sink and regenerative cooling, and outlines a preliminary architecture of the first modular engine prototype.

1. Introduction

Space propulsion is a cornerstone of modern spaceflight, enabling orbital transfers, attitude control, station keeping, and other essential orbital manoeuvres. Within this domain, bipropellant systems have long played an essential role in high-performance applications due to their improved efficiencies over monopropellant thrusters.

Historically, hydrazine-based bipropellants have been the system of choice due to their high energy density, storability, and operational reliability. Most of these propellant combinations, such as hydrazine and nitrogen tetroxide, exhibit a hypergolic behaviour by self-igniting upon contact, offering spontaneous ignition and good propulsive performance. However, the use of these propellants comes at a significant operational and environmental cost. The transport and handling of these highly toxic and carcinogenic substances is dangerous for the personnel and the environment, and requires strict, costly and time-consuming safety protocols to ensure proper decontamination, cleaning of equipment and waste disposal. Furthermore, in 2011 the European Chemical Agency (ECHA) added hydrazine and its derivatives to the candidate list of Substances of Very High Concern (SVHC) under the EU's REACH regulation (Registration, Evaluation, Authorisation and Restriction of Chemicals).[1] This suggested a potential ban on the use of hydrazine in the European Economic Area and prompted a strong response from industry and European national space agencies, which requested and later obtained an exemption from any future REACH authorisation in the case of specific propellant-related applications.[2]

The uncertainty surrounding the future of hydrazine as a propellant for in-space propulsion systems eventually led to significant developments in the field of green propellants. Although a universal definition is yet to be established, green propellants are typically recognised as alternatives to hydrazine and nitrogen tetroxide that offer improvements in terms of safety and storability throughout the various phases of a space mission.

Among the available green propellants, water often stands out as a particularly promising alternative due to its unmatched availability, affordability, chemical stability and non-toxicity. Additionally, water offers opportunities for in-situ resource utilisation (ISRU) and synergies with future human outposts, simplifying refuelling processes and coupling with the Environmental Control and Life Support System (ECLSS).[3] These highly desirable properties have been known since NASA's early days, when the first concepts of Water Electrolysis Propulsion (WEP) systems were proposed.[4] As the name suggests, WEP systems utilise the process of water electrolysis to generate gaseous hydrogen (H_2) and oxygen (O_2) in stoichiometric quantities, which are then burned together in a thruster.

Copyright © 2025 by Faraoni et al. Published by the EUCASS association with permission.

DOI: 10.13009/EUCASS2025-243

Despite the advantages of WEP, its development has historically been hindered by several well-known, system-level limitations. These include the added dry mass of the electrolyser, higher power and thermal demands, rate of production of propellants, concerns about conversion system reliability and increased overall cost. Many of these issues, however, may be offset by the very advantages that make WEP so attractive in the first place. Even more fundamental, and probably harder to overcome, are the intrinsic limitations of gaseous O_2 and H_2: the high stoichiometric combustion temperature and the low density of propellants. These challenges have driven WEP development towards maximum efficiencies, short burn times and consequently low thrust levels. As a result, WEP systems in the 22-500 N range, such as those needed by large spacecraft and space stations, have largely been overlooked by the space industry, research communities, and space agencies.

1.1 Green SWaP Project

To address the limitations of WEP and expand its capabilities to higher thrust levels, the Green SWaP (Green Solar-to-propellant Water Propulsion) project was conceived. Funded by Horizon Europe's European Innovation Council Pathfinder Challenges programme, it is driven by a consortium of leading European universities, research institutions, and industry partners: University of Pisa, Delft University of Technology, University of Turin, Karlsruhe Institute of Technology (KIT), European Research Institute of Catalysis (ERIC) and NOVASPACE.

Green SWaP is based on the innovative idea of converting water into a different combination of propellants: high-concentration liquid hydrogen peroxide (H_2O_2), also known as High-Test Peroxide (HTP), and gaseous hydrogen (H_2). Compared to gaseous oxygen employed in typical WEP, liquid HTP is much denser, leading to improvements in volumetric efficiency. During the four-year duration of the project, the consortium will focus on increasing, up to TRL 4, the necessary technologies for in-space: co-production of H_2O_2 and H_2 from water, concentration of H_2O_2 up to rocket-grade levels, storage of gaseous hydrogen in an inflatable tank, and utilisation of these propellants in two innovative thrusters. One is a small, efficient hydrogen solar thermal thruster for attitude control, while the other is a larger 200 N bipropellant thruster for main propulsion based on HTP and H_2.

1.2 Motivation and Contents

This study is focused on the HTP/GH_2 bipropellant thruster. While HTP/Kerosene and other HTP-hydrocarbon thrusters have been well characterised by multiple research groups, the HTP/GH_2 propellant combination remains largely unexplored. In this engine, HTP is decomposed through a catalytic bed into a high-temperature mixture of superheated H_2O vapor and O_2. When mixed with H_2, the water vapour will dilute the reactants, altering O_2/H_2 ignition characteristics, combustion efficiency, thermal loads, and overall thrust performance. This work quantifies these effects to assess the viability of HTP/GH_2 as a water-based green propulsion solution.

The work is organised as follows: Section 2 outlines the thruster's design and working principles and compares its performance against conventional hydrazine-based systems and the other promising "green" alternatives. Section 3 tackles the ignition problem, assessing whether the pre-ignition mixture can autoignite or would require an external ignition source. Section 4 reports the developments of simplified transient models for radiative, heat-sink, and regenerative cooling. Finally, Section 5 briefly introduces the architecture of the first modular prototype, which will be built and tested at the University of Pisa in the upcoming year.

2. Thruster Architecture and Theoretical Rocket Performance

The concept of HTP-based bipropellant thrusters has long been established in the field of space chemical propulsion. Hydrogen peroxide is a pale blue liquid, slightly more viscous and 40% denser than water. Its molecule is metastable and decomposes exothermically over time into water and oxygen, meaning that pure, anhydrous H_2O_2 cannot be obtained under normal conditions. Aqueous hydrogen peroxide solutions with concentrations above 85% in mass are usually referred to as High-Test Peroxide (HTP). This dense and storable oxidiser has been widely and successfully implemented both as a monopropellant and as an oxidising agent in bipropellant systems. In most of these engines, liquid hydrogen peroxide would not be hypergolic with the fuel if injected directly in the combustion chamber. Instead, HTP is first passed through a catalytic bed to obtain a complete exothermic decomposition, producing a hot gaseous mixture of O_2 and H_2O vapour that reliably ignites the fuel.

Figure 1 illustrates how HTP concentration affects its decomposition temperature and product composition. Higher concentrations yield higher decomposition temperatures and oxygen mass fraction. However, even with 98% HTP the water mass fraction remains significant, exceeding that of the oxygen.

DOI: 10.13009/EUCASS2025-243

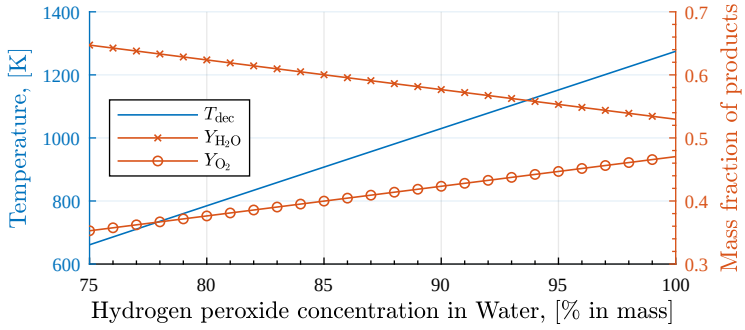


Figure 1: Ideal HTP decomposition temperature and product mass fractions (NASA CEA, T_i=298.15 K, p_c=10 bar).

Building on previous experience, a simplified scheme of the architecture of the HTP/GH_2 thruster is illustrated in Figure 2. It consists of a catalytic bed to decompose HTP, a combustion chamber to burn the decomposition products with hydrogen, and finally a supersonic nozzle to accelerate the flow.

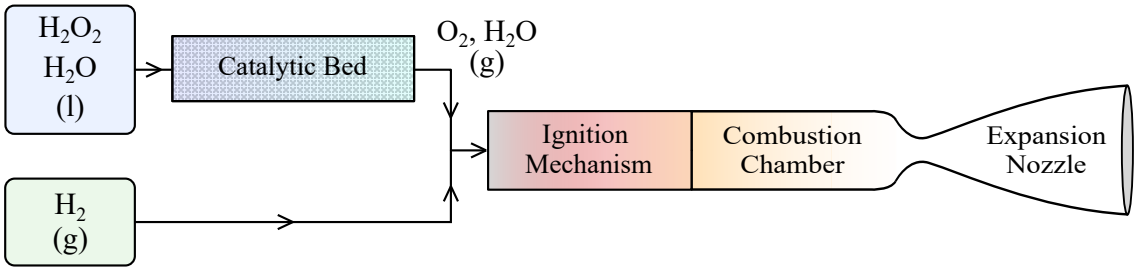


Figure 2: Simplified engine schematic.

Catalytic beds can have different configurations, including metallic gauzes, monolithic structures, and packed beds of granulated pellets, with the latter being the industry standard.[5] A packed-pellet bed usually contains numerous tightly packed spheres (typically 0.1-1 mm in diameter), made of an active catalyst material supported by a base with good thermo-mechanical properties, such as aluminium oxide (alumina, Al_2O_3). For instance, platinum (Pt) is one of the best catalysts for H_2O_2 decomposition, and is usually deposited upon either α-Al_2O_3 (thermodynamically stable, corundum form) or γ-Al_2O_3 (a metastable polymorph, less durable but more porous).

2.1 Performance comparison

The ideal rocket performance of various oxidiser-fuel combinations was obtained by using NASA CEAM (Chemical Equilibrium Applications in MATLAB).[6] Developed at the NASA Lewis Research Center, the Chemical Equilibrium Applications (CEA) was originally written in FORTRAN 77. The present study employs its official MATLAB adaptation, NASA CEAM (still referred to as CEA for brevity), in version 1.3.

The performance comparison was performed using the following CEA settings:

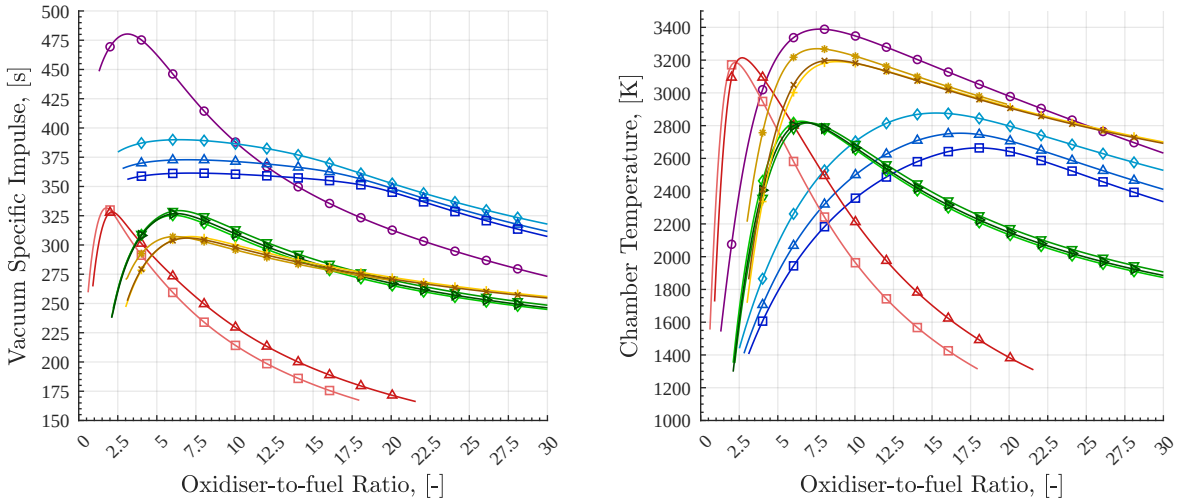
Parameter	Symbol	Value
Infinite Area Chamber	IAC	True
Initial propellant temperature	T_i	298.15 K
Combustion chamber pressure	p_c	10 bar
Expansion area ratio	A_e/A_t	100
Frozen reactions at nozzle throat	nfz	2
Oxidiser-to-fuel ratio	OF	Various values

Table 1: Common input parameters for the performance comparison.

Chamber pressure and expansion ratio were chosen to reflect typical values for 100-500 N thrusters. The specific values are not critical to the analysis, as all propellant combinations are evaluated under identical operating conditions.

DOI: 10.13009/EUCASS2025-243

From NASA CEA calculation and comparison with typical competitors, two performance parameters are illustrated in Figure 3: the vacuum specific impulse and the equilibrium combustion temperature. The former is a metric of fuel efficiency, while the latter can greatly impact the design, operating mode, material selection, and therefore costs, of a thruster.



(a) Vacuum specific impulse

(b) Combustion chamber temperature

Line	Oxidiser	Fuel	Abbreviation	Stoich. OF
	Gaseous Oxygen	Gaseous Hydrogen	GO_2/GH_2	7.94
	98% High-Test Peroxide	Hydrogen	98% HTP/GH_2	17.22
	90% High-Test Peroxide	Hydrogen	90% HTP/GH_2	18.75
	85% High-Test Peroxide	Hydrogen	85% HTP/GH_2	19.85
	Nitrogen Tetroxide	Monomethylhydrazine	NTO/MMH	2.50
	Nitrogen Tetroxide	Unsymmetrical Dimethylhydrazine	NTO/UDMH	3.06
	98% High-Test Peroxide	RP-1	98% HTP/RP_1	7.39
	98% High-Test Peroxide	Propane	98% HTP/C_3H_8	4.52
	98% High-Test Peroxide	Octane (C_8H_{18})	98% HTP/C_8H_{18}	8.08
	Nitrous Oxide	Ethane	N_2O/C_2H_6	10.25
	Nitrous Oxide	Propylene (C_3H_6)	N_2O/C_3H_6	9.41
	Nitrous Oxide	Propane	N_2O/C_3H_8	9.98

Figure 3: Comparison of propulsive performance parameters.

The performance comparison reveals that the H_2O_2/H_2 bipropellant thruster achieves approximately 10% higher specific impulse and 10% lower combustion temperature relative to conventional toxic propellants such as monomethylhydrazine (MMH), unsymmetrical dimethylhydrazine (UDMH), and nitrogen tetroxide (NTO). In addition, the system offers a broad operational range in terms of oxidiser-to-fuel ratio (OF).

Comparing HTP/GH_2 with a conventional GO_2/GH_2 water propulsion system, it is clear from Figure 3a how the latter delivers a superior mass-specific impulse. However, the greater density of liquid HTP more than offsets this drawback, ultimately yielding a superior volumetric efficiency. This can be quantified using the volumetric specific impulse, or density-specific impulse, defined as follows:

$$I_v = g_0\, I_{sp}\, \rho_{eff} = g_0\, I_{sp} \frac{\dot{m}_{fu} + \dot{m}_{ox}}{\dot{m}_{fu}/\rho_{fu} + \dot{m}_{ox}/\rho_{ox}} = g_0\, I_{sp} \frac{1 + OF}{1/\rho_{fu} + OF/\rho_{ox}} \tag{1}$$

Figure 4 shows this comparison of volumetric efficiencies calculated assuming 50 bar, room-temperature gaseous propellant storage. The GO_2/GH_2 propellants are significantly outperformed volumetrically by HTP/GH_2, resulting in a volumetric efficiency approximately 2.5 times higher. In practical terms, this means that for the same propellant tank volume, the H_2O_2/H_2 system may deliver up to 2.5 times more total impulse. This advantage enables greater on-board propellant storage capacity and facilitates the achievement of higher thrust levels within the same volume constraints.

The design point of the thruster can now be selected. As shown in Figure 3a, the best performance would be obtained operating in fuel-rich mixture ratios. However, in the Green SWaP project, both propellants are generated from water in stoichiometric quantities, and the HTP/GH_2 main engine operates alongside a smaller attitude-control

DOI: 10.13009/EUCASS2025-243

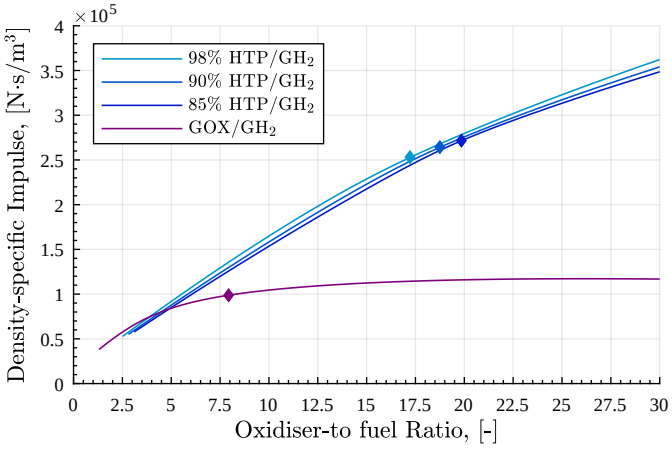


Figure 4: Density-specific impulse vs. OF ratio for water-based propulsion (dots mark stoichiometric mixture).

solar thermal thruster (STT) that consumes hydrogen. These constraints bound the bipropellant thruster to operate in suboptimal, i.e., stoichiometric-to-oxidiser-rich conditions, in order to avoid wasting propellants or having to operate in low-efficiency HTP-monopropellant mode.

Due to the STT's low hydrogen consumption, the HTP/GH_2 engine's nominal OF ratio was set to the stoichiometric value. Note that this value depends on the concentration of hydrogen peroxide, C_{HTP}.

$$\mathrm{OF} = \frac{m_{\mathrm{HTP}}}{m_{\mathrm{H_2}}} = \frac{1}{C_{\mathrm{HTP}}}\frac{m_{\mathrm{H_2O_2}}}{m_{\mathrm{H_2}}} = \frac{1}{C_{\mathrm{HTP}}}\frac{M_{\mathrm{H_2O_2}} n_{\mathrm{H_2O_2}}}{M_{\mathrm{H_2}} n_{\mathrm{H_2}}} \Rightarrow \mathrm{OF}_{\mathrm{sto}} = \frac{1}{C_{\mathrm{HTP}}}\frac{M_{\mathrm{H_2O_2}}}{M_{\mathrm{H_2}}} \tag{2}$$

The higher the concentration of HTP, the higher the propulsive performance. For this reason, the nominal concentration of HTP was set to 98%, with a corresponding stoichiometric OF of around 17.2. This study also considered lower concentrations, down to 85%. The vacuum thrust of the engine was set to 200 N. This value, on the lower end of the 200-500 N class, is suited for orbit-control on large spacecrafts, while remaining a manageable scale for ground testing and early prototype development. Similarly, a nominal combustion chamber pressure of 10 bar and a vacuum expansion area ratio of 300 were selected.

Parameter		**Design point**
Propellants	oxidiser/fuel	98% HTP / H_2
Vacuum Thrust	T	200 N
Oxidiser-to-fuel Ratio	OF	17.22
Chamber pressure	p_c	10 bar
Expansion area ratio	A_e/A_t	300

Table 2: Nominal design point of the HTP/GH_2 thruster.

3. Autoignition Simulations

The HTP/GH_2 propellant combination has received little attention to date compared to classical WEP systems. Therefore, little data exist on this configuration regarding its ignition characteristics and combustion performance. As stated before, in these engines HTP is first decomposed over a catalytic bed into a hot mixture of superheated H_2O vapor and O_2. When this hot oxidiser stream is mixed with gaseous hydrogen in the combustion chamber, self-ignition may occur, removing the need for a dedicated ignition system. However, the considerable amount of H_2O produced by peroxide decomposition mainly acts as both diluent and heat sink at the onset of O_2/H_2 combustion, likely altering the ignition characteristic and combustion efficiency. This study performed a preliminary estimation of autoignition delays and compared them with the corresponding residence times of the flow inside the combustion chamber.

The autoignition delays were calculated by integrating in time a homogeneous chemical reactor model using the Python library Cantera, an open-source, object-oriented software toolkit for chemical kinetics, thermodynamics, and transport processes.[7] A constant pressure reactor was selected, among the numerous types of homogeneous reactors, to simulate the deflagration of the pre-ignition mixture. To simulate the reaction kinetics, Cantera requires a

DOI: 10.13009/EUCASS2025-243

reaction-mechanism file defining all species, elementary reaction steps, thermodynamic data, and transport properties used in chemical-kinetic simulations. This study implemented Cantera's hydrogen-oxygen submechanism *h2o2.yaml*, extracted from GRI-Mech 3.0. This mechanism describes the kinetics and transport of O_2/H_2 combustion using 10 species and 29 elementary reactions, with both ideal-gas and Redlich-Kwong equations of state.[8]

The initial thermodynamic state of this reactor, i.e. of the pre-ignition mixture, was set with enthalpy, pressure and mass fractions. This mixture is the result of an adiabatic and non-reactive mixing of hydrogen gas with the decomposition products of high-test peroxide. Its enthalpy h_{ign} was obtained as follows:

$$h_{\text{ign}} = Y_{\text{ox}} h_{\text{ox}} + Y_{\text{fu}} h_{\text{fu}} = \frac{OF}{1+OF} h_{\text{ox}} + \frac{1}{1+OF} h_{\text{fu}} \tag{3}$$

The pre-ignition pressure p_{ign} was determined using the same throat area A_t and mass flow rate $\dot{m}$ of the bipropellant thruster, but with the characteristic velocity of the pre-ignition mixture c^*_{ign}. As a result, p_{ign} is lower than the nominal chamber pressure of 10 bar, which would only be achieved during steady state combustion. In compact form:

$$p_{ign} = c^*_{ign} \left(\frac{\dot{m}}{A_t} \right)_{\text{biprop}} \tag{4}$$

$$c^*_{ign} = \frac{\sqrt{\gamma \, \mathrm{R}_{ign} \, T_{ign}}}{\gamma} \left(\frac{\gamma+1}{2} \right)^{\frac{\gamma+1}{2(\gamma-1)}} \tag{5}$$

$$\dot{m} = \frac{T}{I_{\text{sp}} \, g_0} \tag{6}$$

The heat capacity ratio γ, the specific gas constant R_{ign}, and the temperature T_{ign} of the pre-ignition mixture were evaluated using Cantera. To do this, the gas object was initialised at a similar pressure, corresponding to monopropellant HTP operation, obtained analogously from Equation 4 using NASA CEA's value of c^*_{mono} and $I_{\text{sp,mono}}$, and with $\dot{m}$ equal to the oxidiser mass flow rate of the bipropellant thruster. This choice has a negligible effect on γ, R_{ign}, and T_{ign}, as these properties depend almost exclusively on the mixture's composition and enthalpy.

The ignition delay can be determined by integrating the reactor over time and monitoring the evolution of either the concentration of some species, the temperature, or the rate of temperature rise. In this study, ignition was identified based on the combustion temperature, with the ignition event being detected once $T > 98\% T_c$. Finally, to achieve a successful thruster ignition, the ignition delay times τ_{ign} must be smaller than the residence time of the pre-ignition mixture inside the combustion chamber, τ_{res}. The latter can be expressed in terms of the chamber characteristic length L^*, set to 1.5 m in this study, and the characteristic velocity c^*_{ign} as follows:

$$\tau_{\text{r}} = \frac{\rho_{ign} V_c}{\dot{m}} = \frac{\rho_{ign} L^* A_t}{p_{ign} A_t / c^*_{ign}} = L^* \frac{c^*_{ign}}{R_{ign} T_{ign}} \tag{7}$$

3.1 Effect of water content on O_2/H_2 autoignition

Before comparing ignition delays to the residence times in the thruster, the influence of water content on autoignition was examined. The O_2/H_2 mixture was held at a stoichiometric ratio while incremental amounts of hot water vapour were added. The temperature of O_2 and H_2O was set, for reference, to the decomposition temperature of 98% HTP.

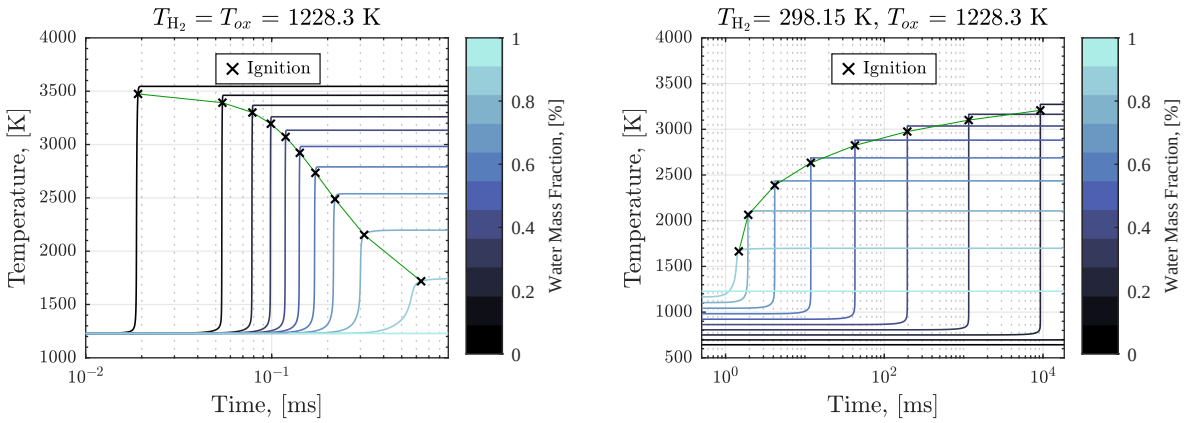


Figure 5: Temperature profiles for stoichiometric $O_2/H_2O/H_2$ autoignition with T_{ox}=1228.3 K and varying $Y_{\text{H}_2\text{O}}$.

Figure 5 illustrates how, when all the species are at the same temperature, higher water content increases ignition delays. Conversely, ignition delays are reduced when considering cold hydrogen, as the greater heat capacity offered by water offsets hydrogen's low temperature. In both cases, the combustion temperature decreases as water is added.

DOI: 10.13009/EUCASS2025-243

3.2 Thruster autoignition delays with ambient temperature propellants

Both gaseous hydrogen and liquid high-test peroxide were initialised at 298.15 K (room temperature). Figure 6 compares the computed autoignition delays τ_{ign} with the corresponding residence times τ_{res} over a wide range of mixture ratios and for three different HTP concentrations. For each HTP concentration, the nozzle throat area was adapted to maintain the same nominal chamber pressure of 10 bar during bipropellant operations.

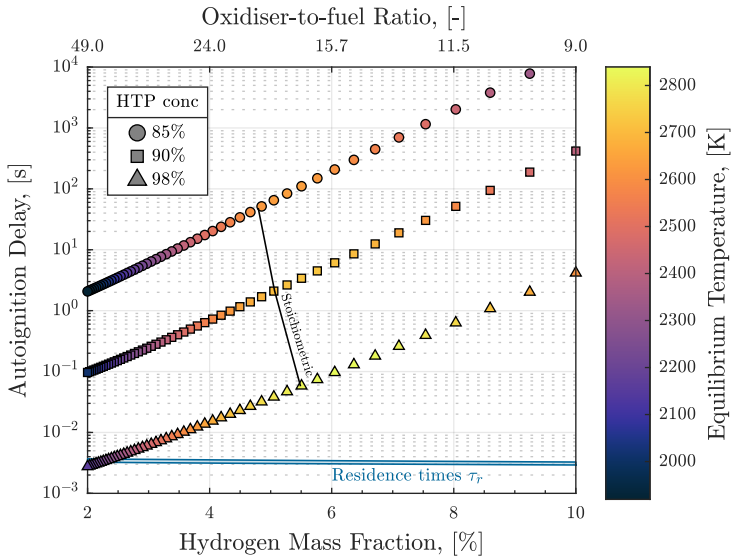


Figure 6: Comparison of autoignition delays and residence times for T_{in}=298.15 K.

Autoignition is successful if the ignition delays are lower than residence times. In this case, ignition delays exceed residence times by a substantial margin. Only 98% HTP at very high OF ratios marginally meets the ignition requirement.

3.3 Effects of hydrogen preheating on autoignition

The impact of hydrogen inlet temperature and chamber pressure on autoignition was evaluated. An increase in H_2 temperature could be obtained through a regenerative cooling system applied to the combustion chamber and nozzle throat, while an increase of pressure could allow improvements in engine performance. This study considered a wide range of initial T_{H_2}, from room temperature to 1500 K.

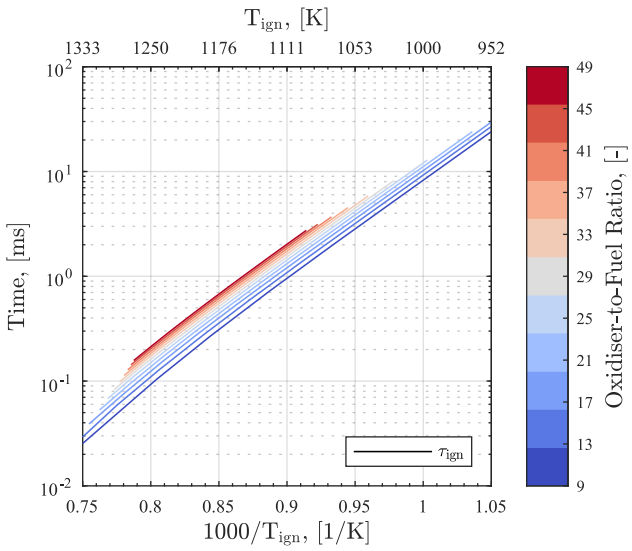


Figure 7: Arrhenius plot for 98% HTP.

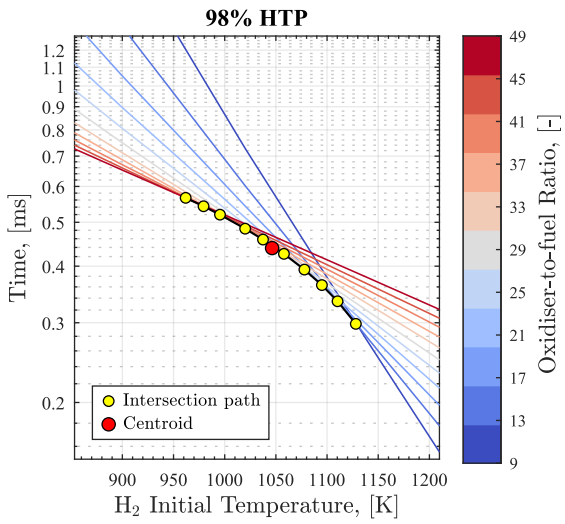


Figure 8: Ignition delays vs. Initial T_{H_2}.

DOI: 10.13009/EUCASS2025-243

The ignition delays reported in Figure 7 exhibit a near-Arrhenius dependence, i.e. $\log \tau_{\text{ign}} \propto 1/T_{\text{ign}}$, consistently with classical combustion theory in the case of a single dominating chain-branching reaction.[9] Under these conditions, these lines have a positive, OF-invariant slope, representing a constant activation energy $-E_a/R_u$.

Plotting $\log \tau_{\text{ign}}$ vs. T_{H_2} also results in almost-straight lines, as shown in Figure 8. In this case, however, the OF ratio changes the slope of the lines, which appear to pivot around a quasi-invariant point, referred to here as the *centroid*. However, the intersections of these lines do not coincide exactly, so the centroid temperature was defined as the mean of consecutive intersections, illustrated as yellow dots in Figure 8. At a fixed initial hydrogen temperature, increasing the OF ratio has opposite effects on the ignition delay depending on whether the initial hydrogen temperature is above or below the centroid temperature. When the hydrogen temperature exceeds the centroid one, raising the hydrogen mass fraction (i.e., reducing OF) accelerates autoignition. Importantly, the centroid temperature determined in this manner is lower than the decomposition temperature of HTP.

Figure 9 presents the results corresponding to three additional HTP concentrations.

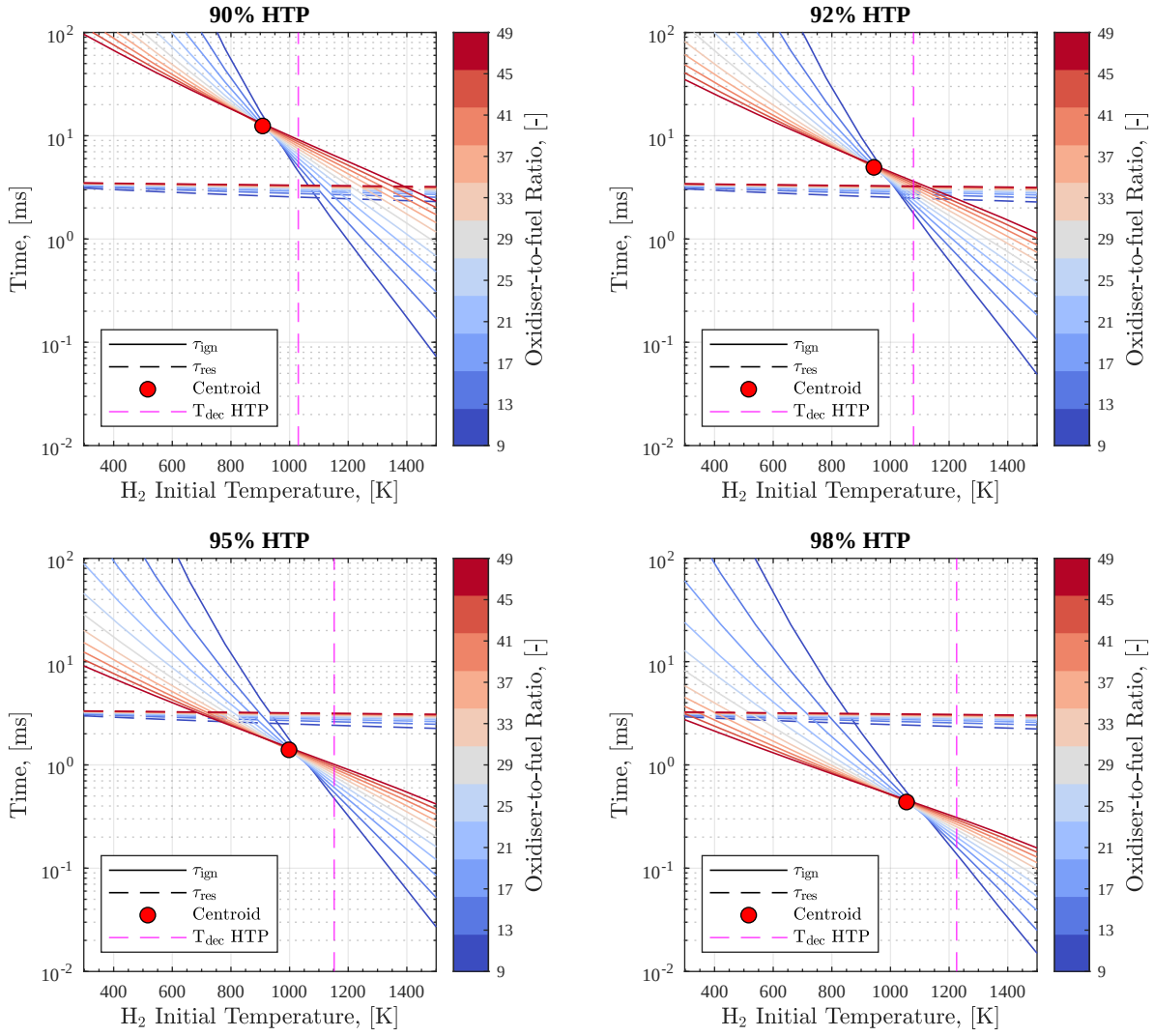


Figure 9: Effects of initial T_{H2} on ignition delays and residence times.

Higher peroxide concentrations lead to lower ignition delays. Furthermore, the centroid temperature increases linearly with the concentration of hydrogen peroxide, as illustrated in Figure 11.

The minimum initial hydrogen temperature is defined as the temperature at which the ignition delay falls below the corresponding residence time. By identifying the intersection points between each pair of τ_{ign} and τ_{res} lines in the preceding plots, the curves of the minimum hydrogen temperature required to achieve autoignition were calculated. These relationships are illustrated in Figure 10.

DOI: 10.13009/EUCASS2025-243

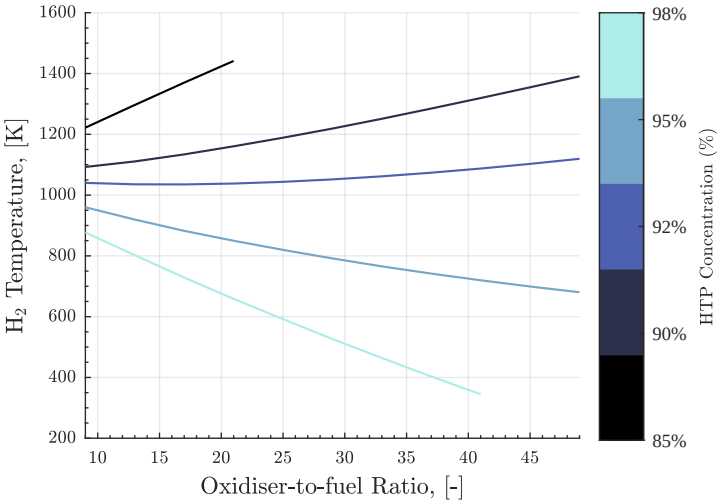


Figure 10: Minimum initial H_2 temperature required for autoignition in the HTP/GH_2 thruster assuming L*=1.5 m and p_c = 10 bar.

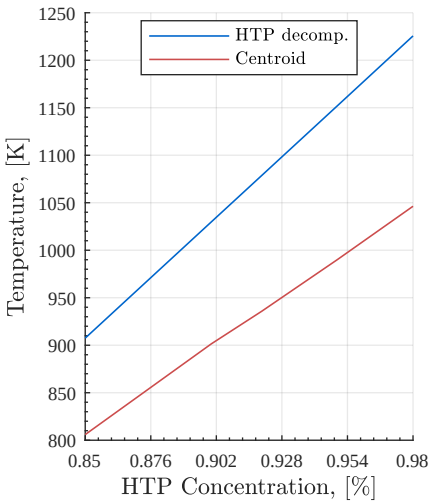


Figure 11: Temperature comparison between HTP decomposition and centroid.

Figure 10 shows a change in slope sign occurring at approximately 92% HTP. This behaviour results from the centroid point dropping below the residence-time curves, as illustrated in Figure 9; consequently, the τ_{ign}/τ_{res} intersections shift to conditions where increasing the OF ratio favors autoignition, indicating that the hydrogen temperature is no longer sufficient to promote it.

3.4 Effects of chamber pressure on autoignition

The influence of nominal chamber pressure on autoignition was also examined. Using the same methodology as previously described, the minimum initial hydrogen temperature required for autoignition was determined for each nominal bipropellant chamber pressure p_c. The results of varying chamber pressure, analogous to those in Figure 10, are presented in Figure 12 for three values of p_c.

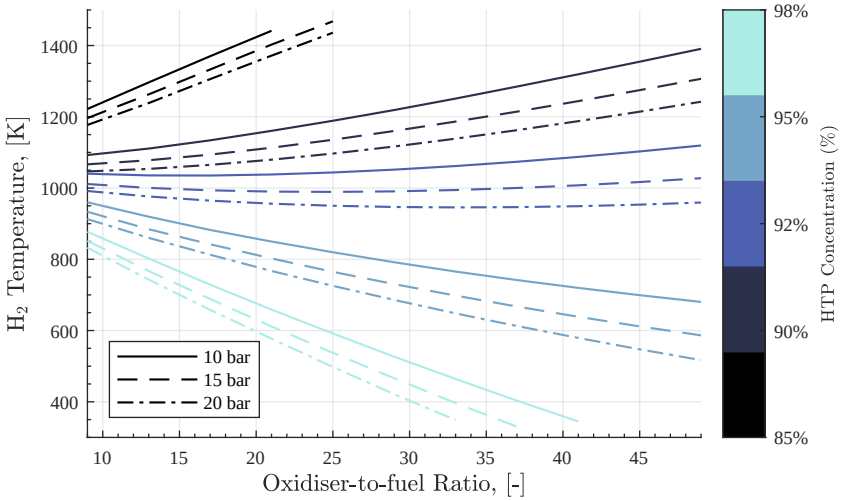


Figure 12: Minimum initial H_2 temperature required for autoignition at various chamber pressures.

Higher chamber pressures consistently shorten ignition delays, thereby reducing the minimum initial hydrogen temperature required for autoignition. Consequently, the maximum attainable chamber pressure is governed by the thermal-structural limits of the thruster components.

DOI: 10.13009/EUCASS2025-243

4. Combustion Chamber Cooling

The stoichiometric combustion temperatures of HTP/GH_2 obtained in Section 2.1 range from around 2600 K to 2900 K, depending on the concentration of HTP. Although these temperatures are relatively low compared to those of other propellant combinations, such as GO_2/GH_2 and MMH/NTO, they surpass the allowable operating temperatures of common wall materials. Numerous cooling techniques can be employed to maintain the wall temperature below specified values, with different levels of complexity and effects on propulsive performance. Sizing the walls of a thruster and selecting the appropriate wall materials requires accurate thermal modelling to account for both the loss in structural strength and the onset of thermal stresses within the walls.

For this reason, transient reduced-order numerical models are being developed to evaluate the application of radiative cooling, heat-sink cooling, and regenerative cooling to the thruster at hand. Radiative cooling, commonly used in flight models operating in vacuum, relies on thin walls made of expensive high-temperature materials, which dissipate heat by radiation to the surroundings. Heat-sink cooling, typical of ground-test prototypes, relies on the thermal inertia of thick chamber walls to absorb heat over short burn durations. Finally, regenerative cooling circulates a fluid through the chamber walls, enabling longer firings. In fully-regenerative cooling, the propellant itself serves as coolant, recovering the absorbed heat and reducing performance loss. In preliminary experiments, regenerative cooling is often implemented in an open loop (active cooling), using water as coolant. This section summarises the ongoing development of such thermal models, with an outlook on future experimental campaigns.

4.1 Radiative-convective 1D heat conduction model

This model describes the one-dimensional, unsteady heat conduction through a flat chamber wall. On the hot-gas side, radiative and convective heat fluxes are applied under the assumptions of optically thin, fully developed, turbulent combustion with unitary enclosure view factor. On the external wall, outgoing radiative and convective heat fluxes are applied. This translates into a boundary value problem in terms of the wall temperature T_w, governed by the elliptic, partial differential equation of heat conduction, subject to a uniform initial condition and two boundary conditions imposed on the internal and external wall.

$$\frac{1}{\alpha}\frac{\partial T_w}{\partial t} = \frac{\partial^2 T_w}{\partial x^2} \tag{8}$$

$$\begin{aligned} T_w(x,0) &= T_{w_0}, && (t=0) \\ h_i(T_{g_a} - T_{w_i}) + \frac{\sigma(T_g^4 - T_{w_i}^4)}{\frac{1}{\varepsilon_{w_i}} + \frac{1}{\varepsilon_{g_w}} - 1} &= -k \left.\frac{\partial T_w}{\partial x}\right|_{x=0}, && (x=0), \\ h_e(T_{w_e} - T_e) + \varepsilon_{w_e}\,\sigma(T_{w_e}^4 - T_e^4) &= -k \left.\frac{\partial T_w}{\partial x}\right|_{x=b}, && (x=b). \end{aligned} \tag{9}$$

In the case of flat-wall heat conduction, the steady-state solution $\bar{T}_w$ is linear in the spatial coordinate x, and defined in terms of the internal and external steady-state wall temperatures, $\bar{T}_{wi}$ and $\bar{T}_{w_e}$.

$$\frac{1}{\alpha}\frac{\partial T_w}{\partial t} = 0 \quad \Rightarrow \quad \frac{\partial^2 T_w}{\partial x^2} = 0 \quad \Rightarrow \quad \bar{T}_w(x) = \bar{T}_{w_i} + \frac{\bar{T}_{w_e} - \bar{T}_{w_i}}{b}x \tag{10}$$

The two unknown temperatures can be obtained by imposing the steady-state boundary conditions, i.e., by solving the following nonlinear system of equations:

$$\begin{cases} h_i(T_{g_a} - T_{w_i}) + \dfrac{\sigma(T_g^4 - \bar{T}_{w_i}^4)}{\frac{1}{\varepsilon_{w_i}} + \frac{1}{\varepsilon_{g_w}} - 1} = -k\dfrac{\bar{T}_{w_e} - \bar{T}_{w_i}}{b} \\ h_e(\bar{T}_{w_e} - T_e) + \varepsilon_{w_e}\,\sigma(\bar{T}_{w_e}^4 - T_e^4) = -k\dfrac{\bar{T}_{w_e} - \bar{T}_{w_i}}{b} \end{cases} \tag{11}$$

This problem could also be expressed in cylindrical coordinates. In this study, the flat-wall model is adopted as it provides more conservative predictions and aligns with the flat-wall approach used by commercial software such as RPA (Rocket Propulsion Analysis),[10] facilitating direct comparison.

DOI: 10.13009/EUCASS2025-243

The convective heat transfer coefficient on the hot-gas side is described by Bartz equation:[11]

$$h_i = h_i(z,\, T_{w_i},\, T_{t_g}) = \frac{0.026\, D_T^{-0.2} \left(\frac{\mu^{0.2} c_p}{Pr^{0.6}}\right)_t \left(\frac{\dot{m}}{A_t}\right)^{0.8} \left(\frac{D_t}{r_{c_t}}\right)^{0.1} \left(\frac{A_t}{A(z)}\right)^{0.9}}{\left[\frac{1}{2}\frac{T_{wi}}{T_{t_g}}\left(1 + \frac{\gamma-1}{2} M^2(z)\right) + \frac{1}{2}\right]^{0.8-\omega/5} \left(1 + \frac{\gamma-1}{2} M^2(z)\right)^{\omega/5}} \tag{12}$$

where ω is the exponent in the viscosity law $\mu \propto T^{\omega}$. This study assumes $\omega = 0.6$, as suggested by literature.[12]

Knowing the geometry of the thruster, i.e. A/A_t, where A_t is the throat area, the mach number M can be obtained from classical gas dynamics theory.[13] Assuming frictionless, adiabatic flow, the following non-linear equation can be solved at all cross-sections.

$$\frac{A(z)}{A_t} = \frac{1}{M(z)} \left[\frac{2}{\gamma+1}\left(1 + \frac{\gamma-1}{2} M^2(z)\right)\right]^{\frac{\gamma+1}{2(\gamma-1)}}. \tag{13}$$

The adiabatic wall temperature T_{g_a} is expressed in terms of the total gas temperature T_{t_g} and the recovery factor r, which in turn can be approximated as an exponential of the Prandtl number:[12]

$$T_{g_a} = T_g + r\frac{1}{2}\frac{\bar{u}^2}{\bar{c}_p} = T_{t_g}\left[\frac{1 + r\left(\frac{\gamma-1}{2}\right)M^2}{1 + \left(\frac{\gamma-1}{2}\right)M^2}\right] \approx T_{t_g}\left[\frac{1 + \mathrm{Pr}^{0.33}\left(\frac{\gamma-1}{2}\right)M^2}{1 + \left(\frac{\gamma-1}{2}\right)M^2}\right] \tag{14}$$

A preliminary configuration of the prototype thruster for the atmospheric test campaign was sized using the software Rocket Propulsion Analysis. A constant thickness of 1 cm, well above the minimum structural requirement, was selected to serve as an effective heat sink during in short firings. The reference material for the chamber walls is AISI 316 stainless steel, which offers a favourable balance of mechanical strength and cost. The prototype design is still in progress; these values are provisional and serve only to verify the steady-state fidelity of the thermal model.

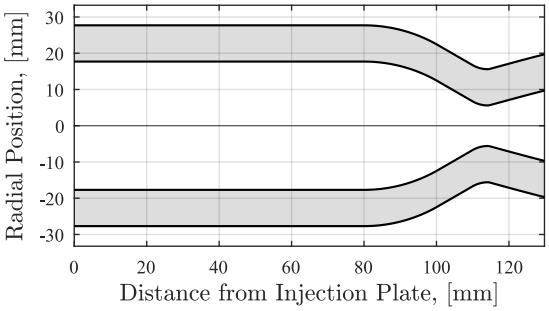


Figure 13: Example geometry for model validation, $L^* = 1$ m, $A_e/A_t = 3$, $A_c/A_t = 10$, b = 10 mm.

Other physical properties were assumed constant and equal to the values reported in Table 3, which have been obtained from literature, NASA CEA and RPA.

Table 3: Summary of parameters used in the combustion chamber cooling validation

Parameter	Symbol	Value	Units
Gas emissivity (H_2O vapour)	ε_{wg}	0.02	-
Inner wall emissivity (AISI 316)	ε_{wi}	0.60	-
Outer wall emissivity (AISI 316)	ε_{we}	0.60	-
Thermal conductivity (AISI 316)	k	22	W m^{-1} K^{-1}
Thermal diffusivity (AISI 316)	α	5×10^{-6}	m^2/s
Wall thickness	b	10	mm
Initial wall temperature	$T_{w,0}$	300	K
Ambient temperature	T_e	300	K
Characteristic velocity	c^*	1854	m/s
Heat-capacity ratio	γ	1.14	-
Specific heat capacity	c_p	3.127×10^3	J kg^{-1} K^{-1}
Prandtl number	Pr	0.772	-
Dynamic viscosity	μ	9.45×10^{-5}	kg m^{-1} s^{-1}

DOI: 10.13009/EUCASS2025-243

The results of this first calculation are shown in Figures 14-18. Good agreement is observed between the present model and RPA's steady-state solution. Only minimal deviations in convective heat flux, due to the slightly different internal wall temperatures, occur in the cylindrical part of the combustion chamber. This is likely due to the assumption of constant physical properties of the internal hot gas, and does not concern the throat section, which is more critical.

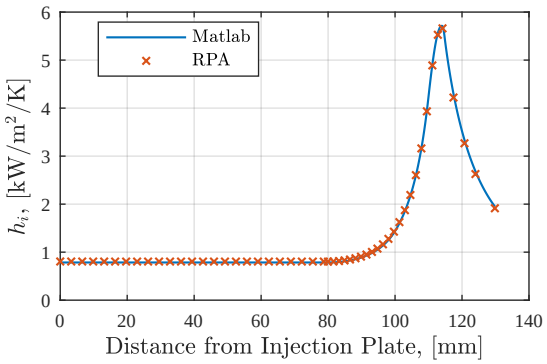


Figure 14: Internal convective heat transfer.

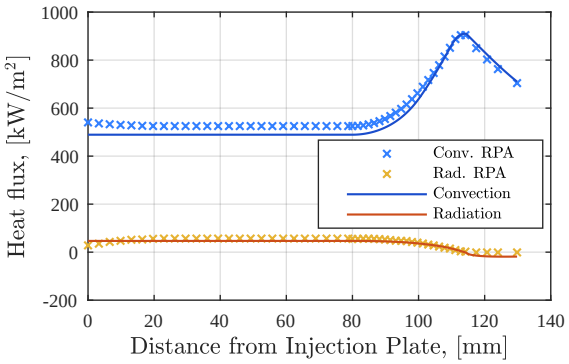


Figure 15: Internal convective and radiative heat fluxes.

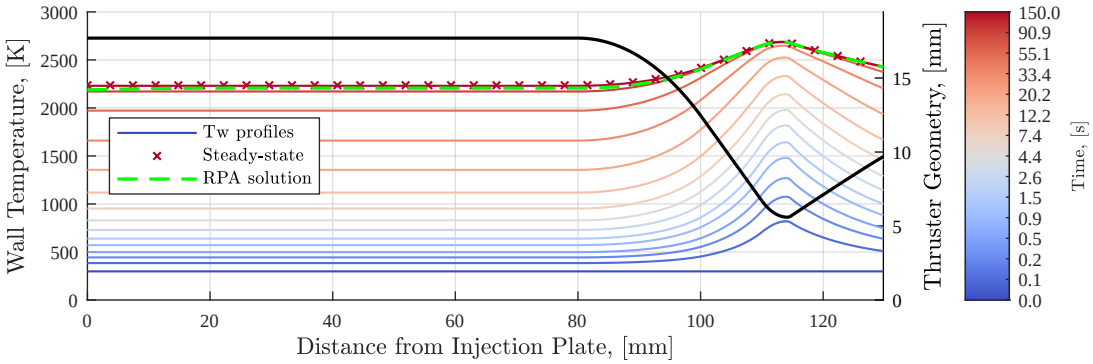


Figure 16: Internal wall temperature evolution and comparison with RPA.

The transient behaviour follows physical expectations: an initial rapid rise in wall temperatures is followed by a gradual approach to the steady-state profile. Heat first accumulates on the inner wall, and then propagates through the remaining thickness, with the throat region experiencing the most severe thermal loads.

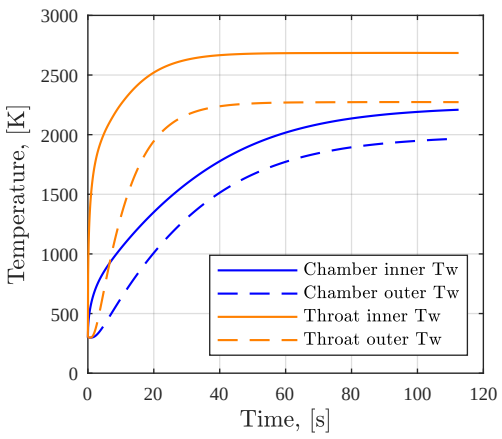


Figure 17: Throat and chamber temperatures.

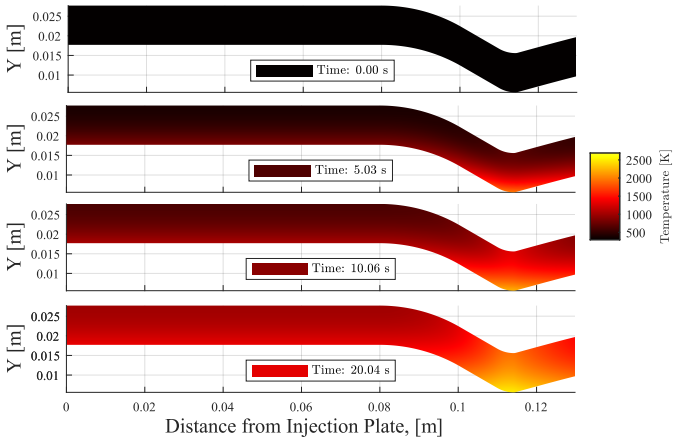


Figure 18: Wall temperatures evolution.

DOI: 10.13009/EUCASS2025-243

4.2 Regenerative cooling

This section reports an update on the development of an in-house regenerative cooling model. In this preliminary phase of the project, the objective is to characterise propellant ignition and combustion efficiencies. Achieving steady-state operation using, for example, open-loop active cooling with liquid water, would facilitate these studies. Accordingly, the model presented in the previous section has been extended to incorporate the transient dynamics of the coolant flow. The problem of heat conduction inside the chamber walls was coupled with the evolution of coolant temperature along the axis of the thruster. The latter can be obtained from the integral form of the total enthalpy balance:

$$\int_V \frac{\partial(\rho\, h_t)}{\partial t}\, dV \;+\; \oint_S \rho\, h_t\, \mathbf{u}\cdot d\mathbf{S} \;=\; \int_V \frac{\partial p}{\partial t}\, dV \;+\; \oint_S \mathbf{u}\cdot(\boldsymbol{\tau}\cdot d\mathbf{S}) \;+\; \int_V \rho\, \mathbf{g}\cdot\mathbf{u}\, dV \;-\; \oint_S \dot{\mathbf{q}}\cdot d\mathbf{S} \;+\; \int_V \dot{Q}\, dV \tag{15}$$

Applied to an infinitesimal annular slice of radius r, height c_h and width ds, and neglecting smaller contributions such as pressure-work, viscous-stresses, gravity, and volumetric heat sources, this simplifies to:

$$\frac{\partial\,(\rho h_t)}{\partial t} 2\pi r c_h\, ds + \dot{m}_r\, dh_t = \dot{q}_w 2\pi r\, ds \tag{16}$$

Finally, substituting $\dot{m}_r = \rho_r u_r A_c$ and $ds = dz\sqrt{1 + (dr/dz)^2}$, and imposing incompressibility, yields:

$$\frac{\partial T_r}{\partial t} + \frac{u_r}{\sqrt{1 + (dr/dz)^2}} \frac{\partial T_r}{\partial z} = \frac{h_r}{\rho_r c_p c_h}\,(T_{w_e} - T_r) \tag{17}$$

Subject to the following initial and boundary conditions:

$$T_r\,(t = 0) = T_{r_0}(z) \quad \text{Initial profile} \tag{18}$$

$$T_r\,(z = z_{\text{in}}) = T_{r_{in}}(t) \quad \text{Inlet temperature} \tag{19}$$

This initial value problem for the one-dimensional, first-order PDE governing the coolant temperature T_r was solved via the method of lines. The spatial domain $z \in [0, L]$ was partitioned into N_z nodes and the spatial derivative was replaced by finite differences, thereby converting the PDE into a system of N_z coupled ordinary differential equations in time. In this study the spatial derivative was approximated with a first-order upwind scheme.

$$\frac{dT_{r,i}}{dt} + \frac{u_r}{\sqrt{1 + \left(\frac{r_i - r_{i-1}}{z_i - z_{i-1}}\right)^2}} \frac{T_{r,i} - T_{r,i-1}}{z_i - z_{i-1}} = \frac{h_r}{\rho_r\, c_p\, c_h}(T_{w_e,i} - T_{r,i}), \qquad i = 2, 3, \ldots, N_z, \tag{20}$$

$$T_{r,1}(t, z = 0) = T_{r_{\text{in}}}(t), \qquad \text{(inlet BC)} \tag{21}$$

$$T_{r,i}(t = 0,\, z) = T_{r_0}(z_i), \qquad i = 1, 2, \ldots, N_z. \tag{22}$$

Although the first-order upwind scheme is only $O(\Delta z)$ accurate and introduces artificial diffusion, pairing it with an implicit time integrator renders the overall method unconditionally stable, thereby eliminating the need to satisfy the Courant-Friedrichs-Lewy constraint ($u_r\,\Delta t/\Delta z < 1$) to prevent the growth of numerical instabilities.[14] To ensure this stability, the ODE system was solved using MATLAB's implicit `ode15s` integrator.

The heat-conduction problem in the chamber walls for T_w and the advection-reaction problem for the coolant T_r were solved sequentially, with the temperature field from one solution providing the boundary condition for the other. Numerical convergence was assessed by monitoring the maximum steady-state difference between the conductive and convective heat fluxes at the outer wall of the chamber. Convergence was declared with a relative error lower than 1%.

The model allows both counterflow and co-flow cooling configurations, as well as axial variations in channel height c_h and wall thickness b. The model is currently limited to incompressible working fluids such as liquid water, and employs the same conductive heat transfer coefficient relation used by RPA.[15]

Figures 19-22 illustrate some preliminary results for a representative configuration with counterflow coaxial-shells cooling using liquid water. An inner wall thickness of 5 mm, constant channel height of 2 mm, coolant mass flow rate of 1 kg/s and initial temperature of 298.15 K were selected. At this stage, these results are intended to demonstrate the convergence of the model and to validate its steady-state results against RPA.

The numerical method converged in less than 10 iterations, and successfully matched the steady-state heat fluxes and wall-temperature predicted by RPA under identical boundary conditions, with negligible deviations across most of the domain. Small discrepancies appear in the coolant temperature profiles, with peak differences of around 1.5% most likely attributable to the assumption of constant coolant properties throughout the thruster. Overall, the transient results exhibit the expected physical behaviour of a counterflow regenerative-cooling system: as the coolant flows, it heats up with a steeper temperature gradient in the throat region, and the resulting temperature difference between the inner and outer chamber walls is large and sustained even at steady state, unlike in the heat-sink cooling case (Fig. 18).

DOI: 10.13009/EUCASS2025-243

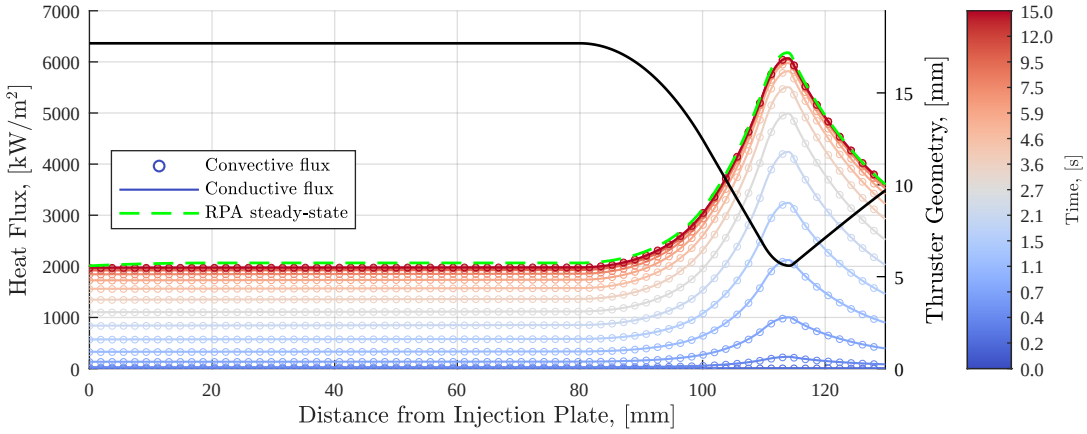


Figure 19: Transient comparison of convective and conductive heat fluxes at $r = r_e$. The convergence of the iterative method is represented by the near-perfect overlap of these two contributions at all time steps and axial positions.

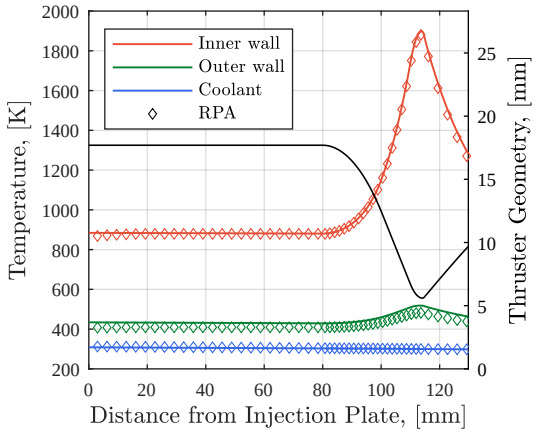


Figure 20: Steady-state temperatures.

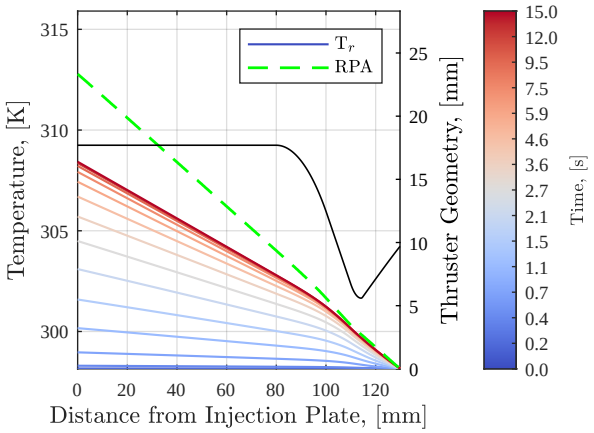


Figure 21: Coolant temperature profiles.

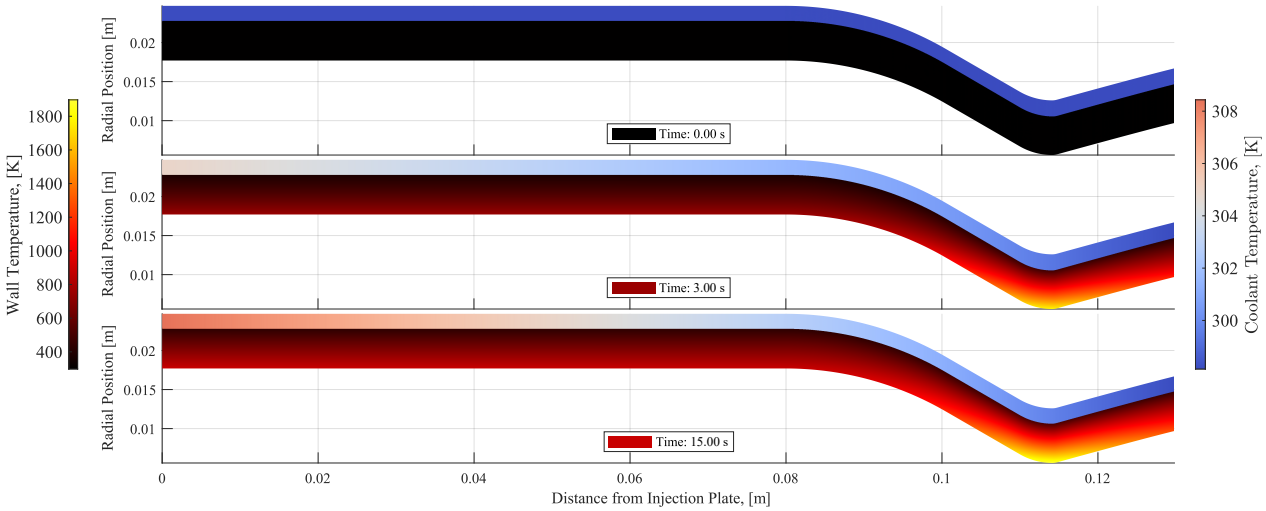


Figure 22: Example of counterflow regenerative cooling with $\dot{m}_r = 1$ kg/s of water at 298.15 K.

DOI: 10.13009/EUCASS2025-243

5. Prototype Development

The first prototype of the bipropellant H_2O_2/H_2 thruster is being designed to support a systematic test campaign aimed at quantifying HTP decomposition, propellant ignition with H_2 and combustion efficiencies across a range of operating conditions. Figure 23 illustrates the modular architecture adopted to enable rapid reconfiguration of key subsystems.

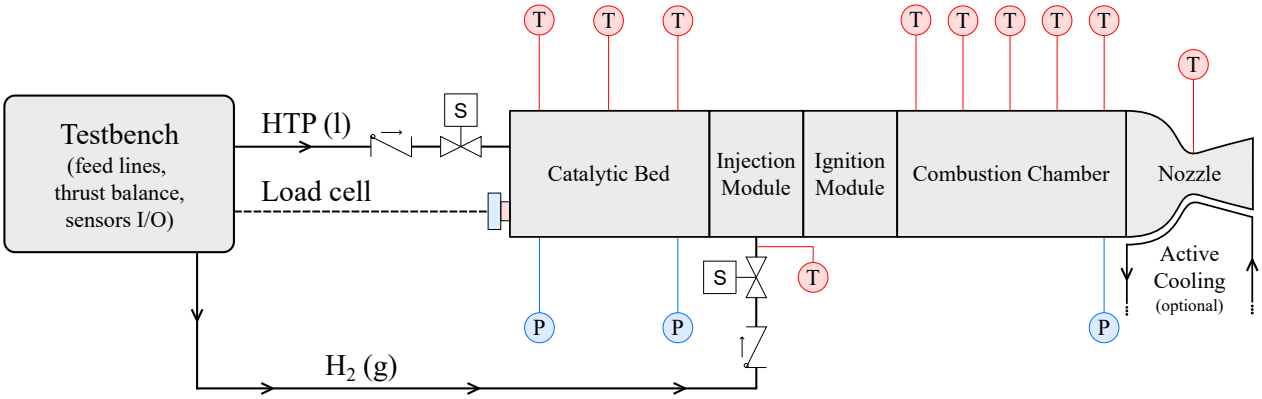


Figure 23: Schematic of the first modular HTP/GH_2 prototype.

6. Conclusions

This study explored the theoretical performance and ignition behaviour of a green bipropellant thruster using high-concentration hydrogen peroxide (HTP) and gaseous hydrogen for innovative water-based space propulsion. Performance predictions indicate that, compared to hydrazine-based bipropellants, HTP/GH_2 operates with 10% lower combustion temperatures while delivering 10% higher specific impulse. Compared to traditional GO_2/GH_2 water propulsion, the reduction in combustion temperature reaches 15%, and despite the greater specific impulse of GO_2/GH_2, the higher propellant density of HTP/GH_2 ultimately results in 2.5 times greater density-specific impulse values. For the same tank volume, this translates into longer firings and less frequent water conversion cycles, or the possibility to operate at higher thrust levels.

Zero-dimensional reaction kinetic simulations indicate that achieving reliable autoignition between HTP decomposition products and gaseous hydrogen could be challenging for room temperature propellants. Preliminary results suggest that autoignition may be feasible with 98% HTP under highly oxidiser-rich conditions, or with the aid of preheated hydrogen and elevated chamber pressures, both of which help in reducing autoignition delays.

Concurrently, transient cooling models are being developed to predict the thruster's startup thermal behaviour. Both the radiative/heat-sink and regenerative cooling models show good agreement with steady-state calculations performed with the software Rocket Propulsion Analysis (RPA). The transient temperature profiles exhibit the expected physical behaviour, with an initial rapid wall-heating phase followed by a gradual approach to equilibrium. The regenerative algorithm converges rapidly in a coaxial-shell configuration assuming incompressible coolant flow.

Future work will focus on refining and validating the ignition and cooling models, as well as on the subsystem design of the first modular engine prototype. Taken together, the results presented in this work highlight the potential of an H_2O_2/H_2 bipropellant thruster as a viable system to extend in-space water propulsion to higher-thrust applications.

7. Acknowledgments

The project leading to this paper has received funding from the European Union under the European Innovation Council grant agreement N. 101161583. Green SWaP, Green Solar-to-propellant Water Propulsion.

Funded by
the European Union

Green
SWaP

University of Pisa
Space Propulsion
Laboratory

The authors also gratefully acknowledge the Space Propulsion Laboratory at the University of Pisa for providing an inspiring research environment and valuable discussions that supported this study.

DOI: 10.13009/EUCASS2025-243

References

[1] ECHA. Inclusion of Substances of Very High Concern in the Candidate List. Helsinki, 2011.

[2] ASD Aerospace - Space Industry Consortium. "Exemption of Propellant-Related Use of Hydrazine and Other Liquid Propellants From the REACH Authorisation Requirement, 2020.

[3] Sam Wilson, Joseph Hunt, Howard Gray, David Gibbon, and Leonard Bauer. Overview of Water Propulsion Developments at Airbus Defence & Space. Glasgow, 2024.

[4] R. J. Rollbuhler. Experimental performance of a water- electrolysis rocket. Technical Report NASA-TM-X-1737, February 1969. Issue: NASA-TM-X-1737 NTRS Author Affiliations: NASA Lewis Research Center NTRS Document ID: 19690009679 NTRS Research Center: Legacy CDMS (CDMS).

[5] Sh. L. Guseinov, S. G. Fedorov, V. A. Kosykh, and P. A. Storozhenko. Hydrogen Peroxide Decomposition Catalysts Used in Rocket Engines. *Russian Journal of Applied Chemistry*, 93(4):467–487, April 2020. Number: 4.

[6] Chemical Equilibrium with Applications in MATLAB (CEAM)(MFS-33320-1) | NASA Software Catalog.

[7] David G. Goodwin, Harry K. Moffat, Ingmar Schoegl, Raymond L. Speth, and Bryan W. Weber. Cantera: An object-oriented software toolkit for chemical kinetics, thermodynamics, and transport processes, 2023.

[8] Cantera, hydrogen-oxygen submechanism extracted from gri-mech 3.0, June 2025. https://github.com/Cantera/cantera/blob/main/data/h2o2.yaml.

[9] Stephen R. Turns and Daniel C. Haworth. *An Introduction to Combustion: Concepts and Applications*. McGraw-Hill, 2012.

[10] A. Ponomarenko. RPA: Design Tool for Liquid Rocket Engine Analysis. 2009.

[11] D. R. Bartz. Turbulent boundary-layer heat transfer from rapidly accelerating flow of rocket combustion gases and of heated air. Technical Report NASA-CR-62615, December 1963. NTRS Author Affiliations: Jet Propulsion Lab., California Inst. of Tech. NTRS Document ID: 19650013685 NTRS Research Center: Legacy CDMS (CDMS).

[12] David H. Huang and Dieter K. Huzel. *Modern Engineering for Design of Liquid-Propellant Rocket Engines*. American Institute of Aeronautics and Astronautics, Washington DC, January 1992.

[13] Jr John D. Anderson. *Modern Compressible Flow: With Historical Perspective*. 2003.

[14] Alfio Quarteroni. *Numerical Models for Differential Problems*. Springer Milan, Milano, 2014.

[15] Alexander Ponomarenko. RPA: Tool for Rocket Propulsion Analysis. Thermal Analysis of Thrust Chambers. 2012.